Montage Operation of Plaquette States in Acoustic Orbital Lattices with Type-III Dirac Points

Qi-Li Sun,[1] Yu-Gui Peng,[1,*] Feng Gao,[1] Bin Li[●],[2] and Xue-Feng Zhu[●][1,†]

[1]*School of Physics and Innovation Institute, Huazhong University of Science and Technology, Wuhan 430074, China*
[2]*School of Mechanical Engineering, Wuhan Polytechnic University, Wuhan 430023, China*

Dispersions around the Dirac points in sonic crystals give rise to various extraordinary transport properties of sound waves. In particular, with tilted Dirac cones, the acoustic Dirac crystals will exhibit obvious anisotropic properties. When the Dirac cone is titled to a certain degree, a unique type-III Dirac point emerges with the extreme anisotropic-wave-transport property, which features the crossing of flat bands and linear dispersions. Recently, some quantum and artificial structures have been proposed to realize different types of Dirac points, where the type-III Dirac point in sonic crystals has rarely been studied so far. Here, we utilize the orbital modes in an acoustic honeycomb lattice to obtain strictly flat bands through eliminating π bonding. The type-III Dirac points emerge with modulated intercell and intracell couplings, which are simulated with specific structural parameters. At type-III Dirac points, the acoustic wave propagation is extremely anisotropic and manifests as plaquette states that exist in the two-dimensional flat-band systems. Inspired by the unique properties at the type-III Dirac points, hybrid acoustic Dirac lattices of regions characterized by different wave-propagation directions are used to conduct the montage operation of plaquette states. The orbital type-III Dirac cones and the montage operation of plaquette states provide opportunities for manipulating energy flow in exotic ways and expanding the potential applications of Dirac materials.

I. INTRODUCTION

Dispersions around the Dirac and Weyl points give rise to extraordinary transport properties of Dirac materials, which have led to significant advances in two-dimensional (2D) materials, such as unconventional Landau levels, Klein tunnels, and weak antilocalization [1,2]. The most vibrant feature of Dirac cones is a conical dispersion with point degeneracies, the robustness of which is protected by topological charges [3,4]. In the reciprocal space, a standard Dirac cone possesses rotational symmetry [5], which can be further tilted, since the stringent Lorentz invariance is absent in a lattice with broken rotational symmetry [6] and has been observed in many Dirac materials, such as strained graphene [7–10]. According to the geometry of Fermi surface and band slopes, Dirac points are classified into different types [5,11]. The cylindrically symmetric dispersion cone is classified as a type-I Dirac cone, as shown in Fig. 1(a); this has identical linear dispersions in all directions and is characterized by a pointlike Fermi surface where the density of states vanishes linearly [12]. If the

Dirac cone is tilted slightly with a broken rotational symmetry, where the Fermi surface is still pointlike, the linear dispersions become anisotropic, as displayed in Fig. 1(b). This type of tilted type-I Dirac point was predicted in quinoid-type and hydrogenated graphene [9,13] and indirectly evidenced in organic semiconductors [14]. When the Dirac cone is further tilted to tip over under the Fermi surface, the Fermi surface becomes two crossing lines; this is termed a type-II Dirac point [Fig. 1(c)]. For the type-II Dirac cone, strong anisotropy emerges on the Fermi surface [6,15,16]. Type-II Dirac points have been observed in 2D semimetals [17] and acoustic metamaterials, which have led to highly anisotropic optical [18], magnetic [19], electrical [20], and acoustic properties [8]. A type-III Dirac point forms between type-I and type-II Dirac points, for which the Dirac cone is critically tilted and just touches the Fermi surface, with a flat band in one direction, as shown in Fig. 1(d). Due to its distinct Fermi surface, diverging density of states, and extreme anisotropy with flat bands [21], the type-III Dirac points have attracted much attention and have been observed experimentally in low-temperature photonic orbital graphene [11]. In previous studies, the type-III Dirac points were constructed by band inversion [11,22] or symmetry perturbation [23]. However, these methods depend on intricately regulated couplings

---
*ygpeng@hust.edu.cn
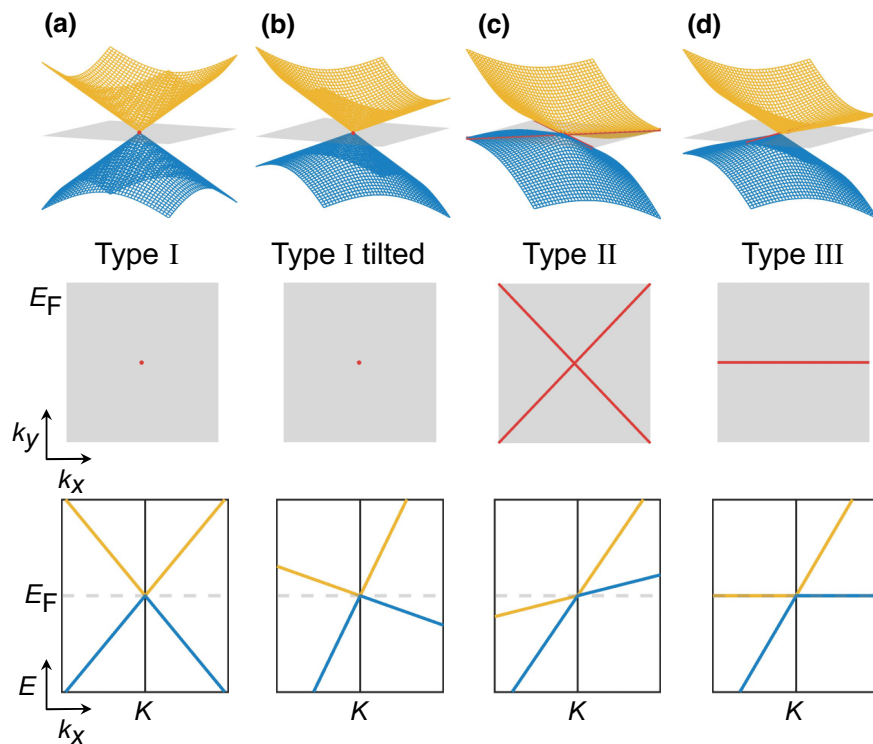†xfzhu@hust.edu.cn

024025-1

FIG. 1. Band structures at different types of Dirac points. Top, band structures and the zero-energy Fermi surface. Middle, isofrequency contours on the zero-energy Fermi surface. Bottom, Dirac dispersions along k_x at $k_y = 0$. (a) Type-I Dirac cone, which has identical linear dispersions in all directions, is characterized by a pointlike Fermi surface. (b) Type-I tilted Dirac cone, which is not rotationally symmetric and linear dispersions are tilted along a specific direction. (c) Type-II Dirac cone, which is formed by a tipped-over cone (highly tilted), resulting in two crossing lines on the Fermi surface. (d) Type-III Dirac cone, which combines the linear dispersions and a flat band on the Fermi surface.

in the lattice [9], generally realized by employing the stratified media [24] or engineering the tight-bonding model [5,9,11], which poses big challenges for artificial materials. Recently, the reported photonic realization [11] paved an explicit path for constructing type-III Dirac points, thanks to the exact controllability of on-site energies and coupling in photonic crystals under extreme conditions [25]. For example, the photonic crystal operates at a very low temperature of about 10 K and employs the embedded quantum wells to realize desired coupling arrangements in type-III Dirac points [11], with an imperfect flat band resulting from unavoidable coupling.

An acoustic lattice provides alternative possibilities to realize strict type-III Dirac points, because of its unique control of couplings related to acoustic field distributions. The acoustic lattice enables specific couplings to be completely eliminated while accurately regulating other couplings, making it feasible to obtain strict flat bands accompanied by dispersive bands and energy inversion. Nonetheless, acoustic realization provides a powerful platform for investigating unusual wave-manipulation properties for the lattice of type-III Dirac points. Here, we present a comprehensive study of acoustic type-III Dirac points. We show the existence of type-III Dirac points in acoustic

orbital lattices by verifying the relationship between the extremely anisotropic field distributions of plaquette states and the band structures. The p-orbital bands are investigated as the eigenmodes of an acoustic honeycomb lattice, which can be simplified as a tight-bonding model [26]. In the 2D orbital lattice, selected couplings between the orbitals orthogonal to the coupling channels ensure strictly flat bands. By breaking the coupling symmetry, mimicking uniaxial strains in graphene [7], energy inversion is implemented to deform the band structures into type-III Dirac points. In addition, we introduce another coupling modulation to maintain the translational lattice symmetry, which makes the connection of multiple type-III Dirac lattices with different anisotropies possible. For a hybrid lattice system of flat bands and type-III Dirac points, the montage operation of plaquette states is also studied by simulations. Our work shows promising prospects of engineering different band structures in the acoustic orbital lattices, which allows for intriguing wave-propagation manipulation, such as acoustic wave routing, splitting, and circulating.

II. THEORY

Due to the favorable features of the graphene lattice in research on Dirac points, a honeycomb p-orbital lattice is
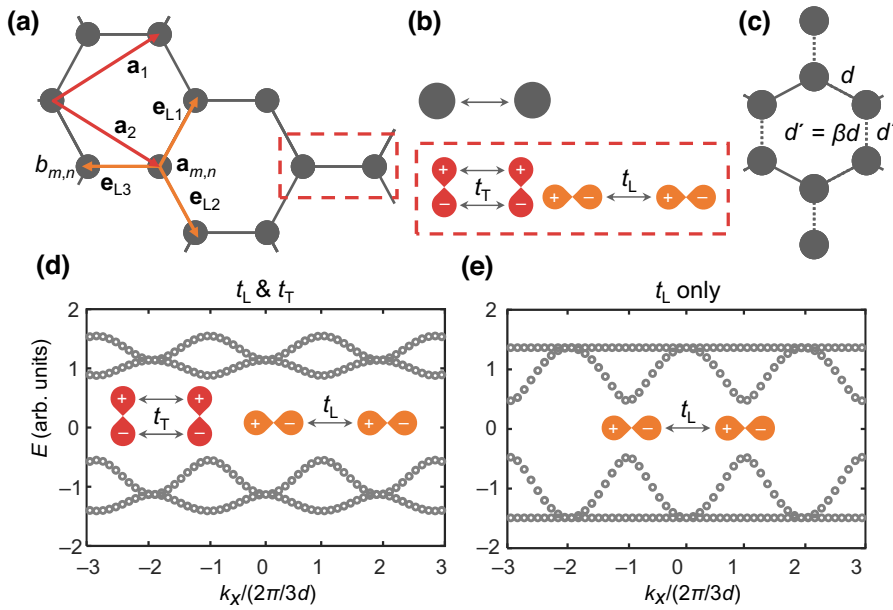
FIG. 2. (a) Schematic of the acoustic orbital lattice model. (b) p-Orbital lattice, in which two different bonding types exist. (c) Configuration of modulated links and fixed links. (d) Band structure with the combined effect of π and σ bonding along the k_x direction at $k_y = 0$. (e) Band structure with only σ bonding along the k_x direction at $k_y = 0$.

employed as the acoustic platform [sketched in Figs. 2(a) and 2(b)]. For the p-orbital modes, there are two bonding types, that is, π bonding and σ bonding [Fig. 2(b)]. The

strengths of π and σ bonding are represented by t_T and t_L, respectively. The tight-bonding Hamiltonian of p_x and p_y modes in the honeycomb orbital lattice can be described
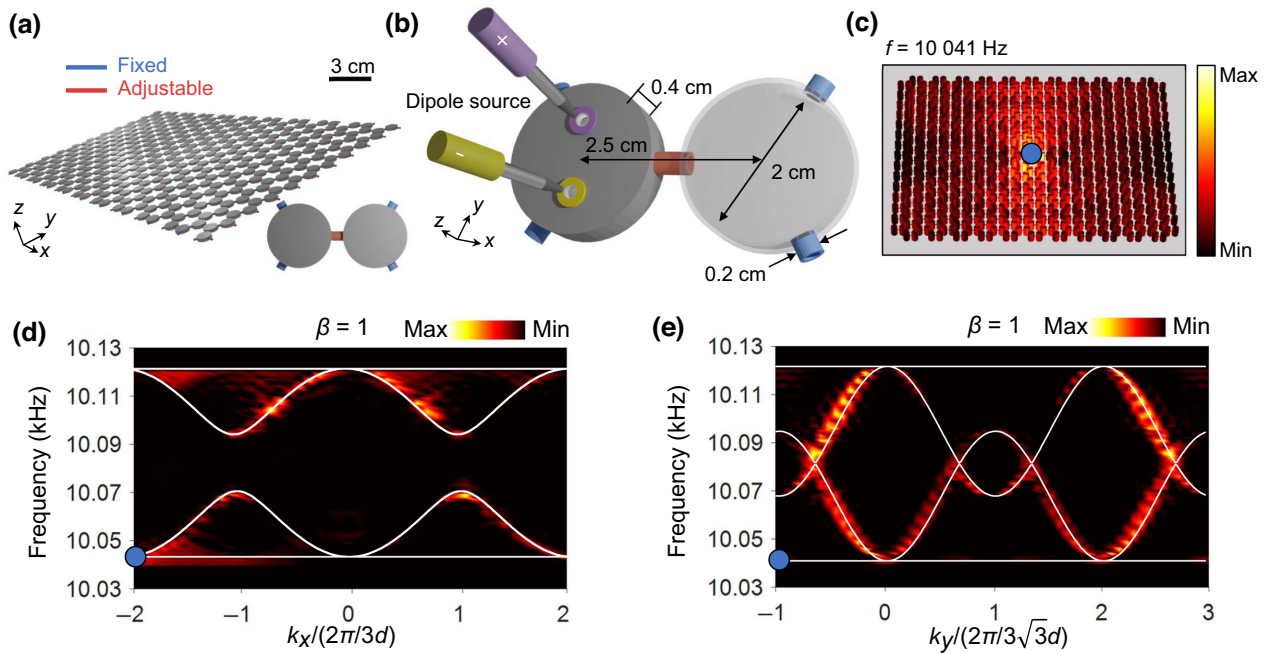

FIG. 3. (a) Schematic of a honeycomb p-orbital lattice, with the coupling tubes in red being adjustable and the tubes in blue being fixed. Gray disks represent cavity resonators. (b) Dipolar source is utilized as the excitation source by utilizing two point sources (yellow and purple) with π-phase difference. By operating the dipolar source, a dipole mode is established in the cavity. Length of the red tube determines the intracell coupling strength, t_L, resulting in deformation of the target bands. Cavity size plays a dominant role in determining the eigenfrequency of modes and the band gap between different modes. (c) Simulated pressure field at 10 041 Hz, with a central excitation in the lattice marked by the blue dot. (d),(e) Fourier spectra along the k_x direction at $k_y = 0$ and along the k_y direction at $k_x = 0$, respectively.
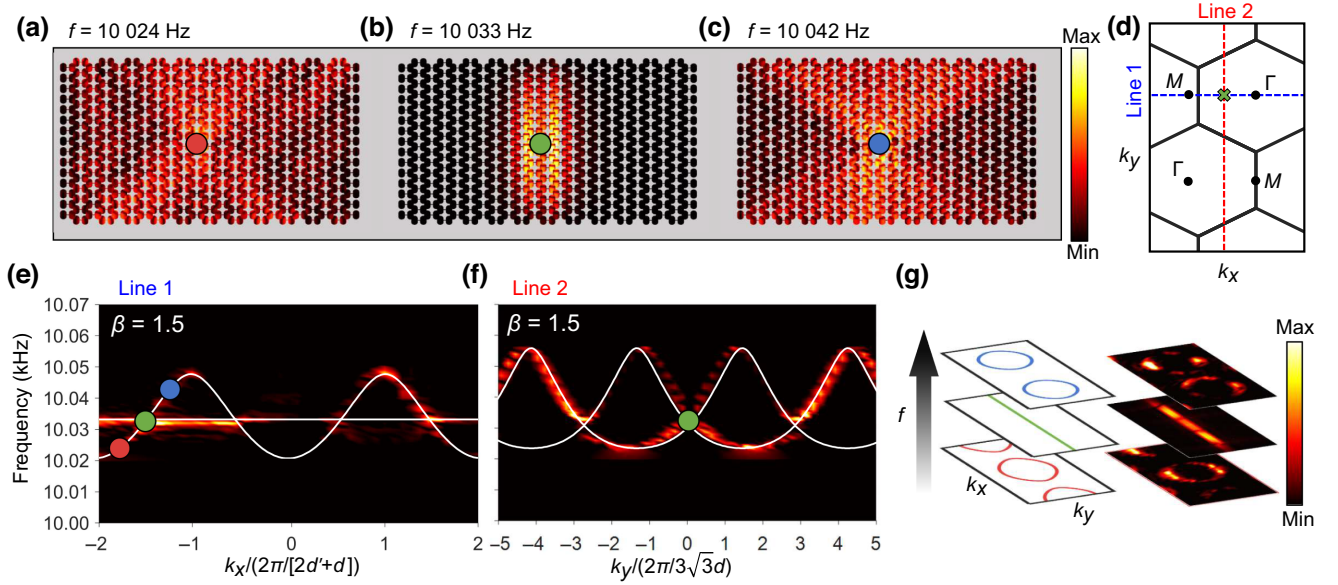
FIG. 4. Type-III Dirac points. Simulated pressure fields at different frequencies below the Dirac point (a), at the Dirac point (b), and above the Dirac cone (c). (d) Reciprocal space of deformed honeycomb lattice. Blue and red lines are sections of extracted Fourier spectra in (e),(f), and crossing point indicates the position of type-Ⅲ Dirac points. (e) Fourier spectrum of modulated orbital lattice along the k_x direction at $k_y = 0$, where red, green, and blue spheres correspond to the cases in (a)–(c), respectively. (f) Fourier spectrum of modulated orbital lattice along the k_y direction at $k_x = 0$, where the Dirac point is marked by the green sphere. (g) Isofrequency contours in reciprocal space at three excitation frequencies (left) and corresponding Fourier spectra (right).

as [27]

$$
\begin{aligned}
H &= \sum_{m,n} -[t_{\mathrm{L}}(\hat{\mathbf{a}}^{\dagger}_{m,n} \cdot \mathbf{e}_{\mathrm{L}1})(\mathbf{e}_{\mathrm{L}1} \cdot \hat{\mathbf{b}}^{\dagger}_{m,n}) \\
&\quad + t_{\mathrm{L}}(\hat{\mathbf{a}}^{\dagger}_{m+1,n} \cdot \mathbf{e}_{\mathrm{L}2})(\mathbf{e}_{\mathrm{L}2} \cdot \hat{\mathbf{b}}^{\dagger}_{m,n}) \\
&\quad + t_{\mathrm{L}}(\hat{\mathbf{a}}^{\dagger}_{m,n+1} \cdot \mathbf{e}_{\mathrm{L}3})(\mathbf{e}_{\mathrm{L}3} \cdot \hat{\mathbf{b}}^{\dagger}_{m,n}) \\
&\quad + t_{\mathrm{T}}(\hat{\mathbf{a}}^{\dagger}_{m,n} \cdot \mathbf{e}_{\mathrm{T}1})(\mathbf{e}_{\mathrm{T}1} \cdot \hat{\mathbf{b}}^{\dagger}_{m,n}) \\
&\quad + t_{\mathrm{T}}(\hat{\mathbf{a}}^{\dagger}_{m+1,n} \cdot \mathbf{e}_{\mathrm{T}2})(\mathbf{e}_{\mathrm{T}2} \cdot \hat{\mathbf{b}}^{\dagger}_{m,n}) \\
&\quad + t_{\mathrm{T}}(\hat{\mathbf{a}}^{\dagger}_{m,n+1} \cdot \mathbf{e}_{\mathrm{T}3})(\mathbf{e}_{\mathrm{T}3} \cdot \hat{\mathbf{b}}^{\dagger}_{m,n}) + \mathrm{H.c.}],
\end{aligned} \tag{1}
$$

where $\mathbf{e}_{\mathrm{L}1,\mathrm{L}2,\mathrm{L}3}$ are the unit vectors oriented parallel to the links between two nearest-neighboring sites in Fig. 2(a). $\mathbf{e}_{\mathrm{T}1,\mathrm{T}2,\mathrm{T}3}$ are the unit vectors oriented perpendicular to $\mathbf{e}_{\mathrm{L}1,\mathrm{L}2,\mathrm{L}3}$, satisfying the right-hand rule. $\hat{\mathbf{a}}^{\dagger}_{m,n} = (\hat{\mathbf{a}}^{\dagger}_{m,n(x)}, \hat{\mathbf{a}}^{\dagger}_{m,n(y)})$ and $\hat{\mathbf{b}}^{\dagger}_{m,n} = (\hat{\mathbf{b}}^{\dagger}_{m,n(x)}, \hat{\mathbf{b}}^{\dagger}_{m,n(y)})$ are the creation operators of resonances in p_x or p_y modes of the a, b sites of the (m, n) unit cell in the lattice. The p-mode band structure is established by employing the Hamiltonian shown in Fig. 2(d), which comprises two sets of touched dispersive bands. The strengths of two respective bonds affect the band structure significantly [28]. If π bonding is totally negligible ($t_{\mathrm{T}} = 0$), the Hamiltonian can be written in **k** space as

$$
H(\mathbf{k}) = -t_L \begin{pmatrix} 0 & C(\mathbf{k}) \\ C(\mathbf{k})^{\dagger} & 0 \end{pmatrix}, \quad C(\mathbf{k}) = \begin{pmatrix} f_1 & g \\ g & f_2 \end{pmatrix}, \tag{2}
$$

where $f_1 = (3/4)(e^{i\mathbf{k}\cdot\mathbf{a}_1} + e^{i\mathbf{k}\cdot\mathbf{a}_2})$, $f_2 = 1 + (1/4)(e^{i\mathbf{k}\cdot\mathbf{a}_1} + e^{i\mathbf{k}\cdot\mathbf{a}_2})$, and $g = \left(\sqrt{3}/4\right)(e^{i\mathbf{k}\cdot\mathbf{a}_1} - e^{i\mathbf{k}\cdot\mathbf{a}_2})$, with the lattice vectors $\mathbf{a}_1 = \left[(3/2)d, \left(\sqrt{3}/2\right)d\right]$ and $\mathbf{a}_2 = [(3/2)d, -\left(\sqrt{3}/2\right)d]$, as depicted in Fig. 2(a), and $\mathbf{k} = (k_x, k_y)$ is the quasimomentum in reciprocal space. Therefore, the band structures of p-orbital lattices are obtained, as shown in Fig. 2(e); these consist of two strictly flat bands with dispersive bands. This arrangement lays the foundation for constructing the type-III Dirac points, for which the energy levels of both flat bands and dispersive bands can be tailored independently, making the flat bands cross at the linear region of the dispersive bands. As a result, both flat bands and linear dispersions are achieved and the type-III Dirac points are then constructed. The deformation of the p-orbital lattice can serve as an effective approach to regulate the band structures [7]; this is equivalent to modulating the bonding strength in certain directions. Here, modulation can be easily operated by adjusting the length of links between two nearest-neighboring sites along a certain direction [11], where the length ratio of the modulated links to the fixed links can be defined by $\beta = d'/d$, as shown in Fig. 2(c), which reflects the coupling-strength ratio between intracell sites and intercell sites [29]. Thus, f_2 in the Hamiltonian of Eq. (2) can be replaced by $f_2 = \beta + (1/4)(e^{i\mathbf{k}\cdot\mathbf{a}_1} + e^{i\mathbf{k}\cdot\mathbf{a}_2})$, with f_1 and g being constant [11]. Therefore, it is feasible to achieve strict type-III Dirac points in a honeycomb p-orbital
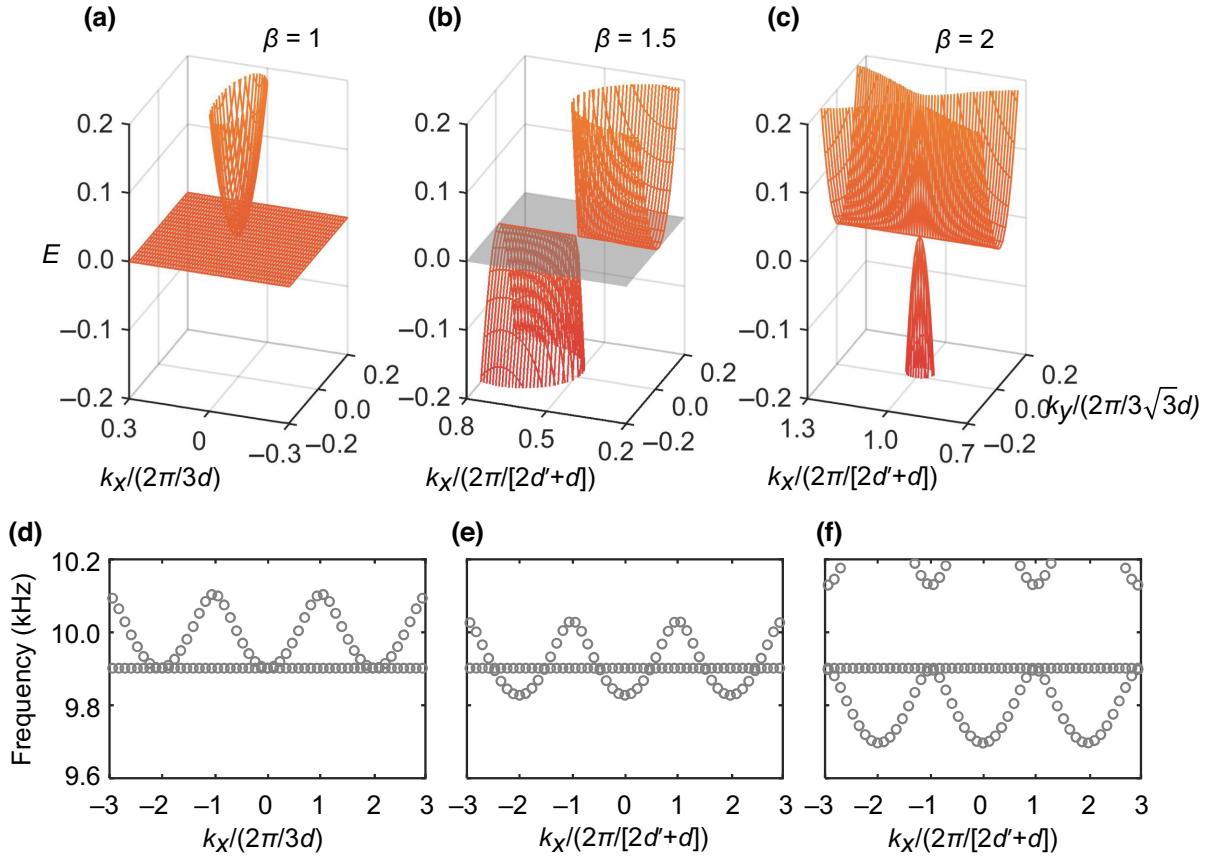
FIG. 5.   Relationship between dispersion and parameter β. (a)–(c) Dispersion diagrams when $\beta = 1$ (no modulation), $\beta = 1.5$, and $\beta = 2$, respectively. (d)–(f) Dispersion curves at the plane of $k_y = 0$ when $\beta = 1$ (no modulation), $\beta = 1.5$, and $\beta = 2$, respectively.

lattice. It should be mentioned that it is very challenging to totally eliminate one specific type of bonding and engineer the other one without any influence. In natural materials, including artificial lattices, the strengths of mode bonding are regulated simultaneously. Nevertheless, the acoustic orbital lattices present an excellent platform for constructing strict type-III Dirac points due to their flexible tunability for different orbital couplings, which offer promising opportunities for manipulating sound-wave propagation.

III. ACOUSTIC TYPE-III DIRAC POINTS

The employed acoustic platform comprises cylindrical resonators coupled by tubes, in which the length of coupling tubes, the axes of which are along the x direction, can be adjusted, with the other tubes fixed. Additionally, the axes of the coupling tubes point to the center of the resonators. The distinct coupling tubes are represented by different colors (red and blue) in Fig. 3(a). The resonators are arranged in the honeycomb configuration to form a graphene lattice. The sizes of resonators and coupling tubes are based on the designed resonant frequencies and bonding strengths. The resonator has a

disk shape, with a diameter that can largely separate the p_x and p_y modes from the p_z mode. Moreover, in the designed orbital lattice, there is only one coupling (i.e., σ coupling) between the neighboring-site cavities. The π coupling does not exist in our case due to the harmonic acoustic field in the resonators, where the coupling tubes are located at the field node. For p-orbital excitation, we utilize a pair of monopole sources with π-phase difference, as sketched in Fig. 3(b).

In an unmodulated orbital lattice ($\beta = 1$), the center-to-center spacing between two coupled cavities is 2.5 cm, the thickness of the cavities is 0.4 cm, the diameter of the resonators is 2 cm, and the diameter of the coupling tubes is 0.2 cm, as shown in Fig. 3(b). The pressure field in the p-orbital lattice is excited at 10 041 Hz, as presented in Fig. 3(c), with the excitation source of y polarization located at the lattice center. The simulations are all conducted with the acoustic module in commercial finite-element software, COMSOL Multiphysics. From the simulated pressure fields at different frequencies, we can further calculate the dispersion spectra via Fourier transformation along the k_x direction at $k_y = 0$ [Fig. 3(d)] and along the k_y direction at $k_x = 0$ [Fig. 3(e)] in reciprocal space. The simulated dispersion spectra (bright strips) agree well with
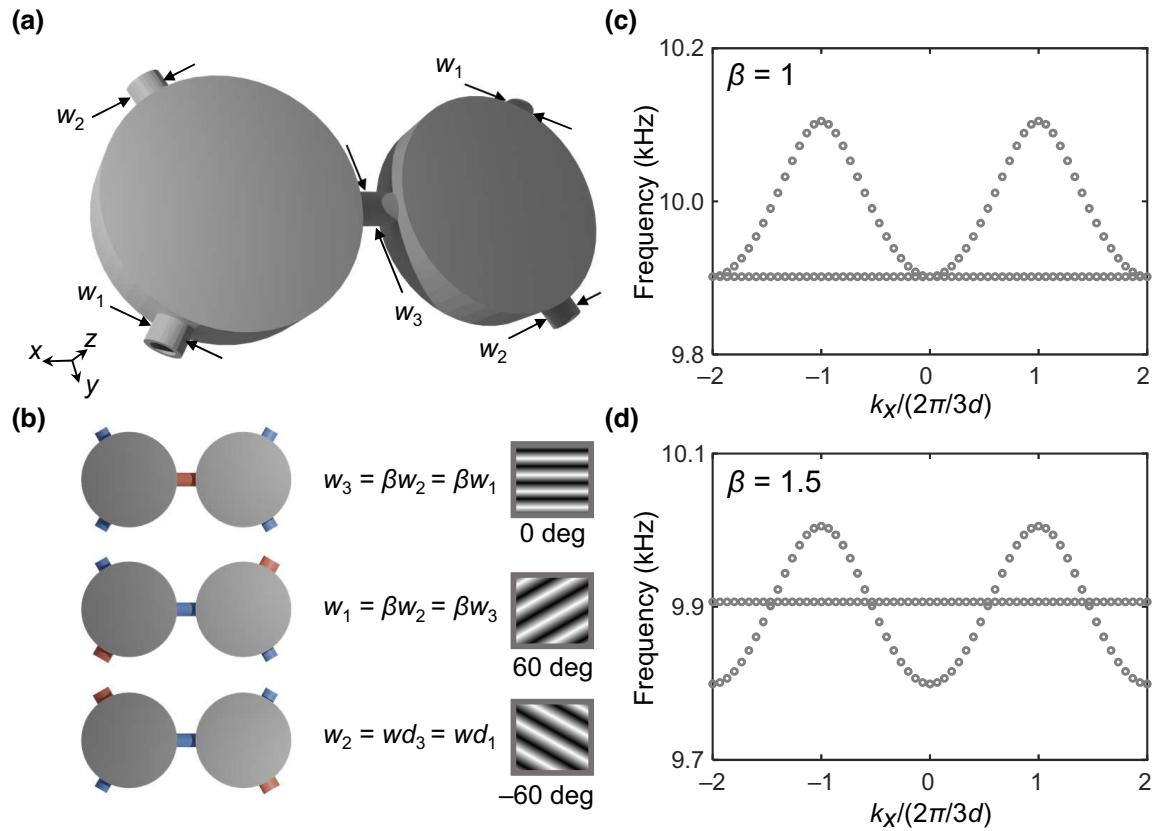
FIG. 6.   Modulated *p*-orbital lattices. (a) Unit cell of the *p*-orbital lattice, in which the coupling tubes are divided into three categories, with tube diameters w_1, w_2, and w_3. (b) Different configurations of modulated unit cells with different principal axes at 0°, 60°, and −60° (right). (c) *p*-Mode dispersion when $\beta = 1$. (d) *p*-Mode dispersion when $\beta = 1.5$ with the existence of the type-III Dirac point.

the calculations (white lines), indicating the existence of a flat band touching a parabolic band.

To investigate the properties of the type-III Dirac point, we tune the coupling ratio to $\beta = 1.5$, which is achieved by adjusting the length of intracell coupling tubes (red) to be 1.5 times longer than the intercell ones (blue). The dipolar sources at different frequencies are placed at the lattice center to excite pressure fields. There are three types of acoustic field distributions, as shown in Figs. 4(a)–4(c). At 10 024 Hz, the frequency is located below the Dirac point with weak anisotropic wave propagation, as shown in Fig. 4(a). At 10 033 Hz, the frequency is located right at the Dirac point with extreme anisotropic wave propagation, as shown in Fig. 4(b), forming the one-dimensional (1D) plaquette states [30]. At 10 042 Hz, the frequency is located above the Dirac point with conical wave propagation, as shown in Fig. 4(c). The spectra in the reciprocal space obtained by Fourier transformation are shown in Figs. 4(e) and 4(f). The results show that the type-III Dirac point exists and features a flat band crossing a linear band along the k_x direction [Fig. 4(e)] and two linear bands crossing along the k_y direction [Fig. 4(f)]. Moreover, we show the spectra in k_x - k_y space with increasing frequencies in Fig. 4(g), where the simulated spectra (bright trips) agree

well with the theoretical isofrequency contours (colored lines). From the isofrequency contours, we can clearly find the directional propagation of 1D plaquette states at the type-III Dirac point and conical wave propagation above the Dirac point.

The evolution of band inversion in the vicinity of the type-III Dirac point is analyzed in Fig. 5 by employing the tight-binding model as a function of β. As the factor β increases from 1 to 2, the calculated bands undergo a transformation from a paraboloid band touched by a plane band at $\beta = 1$ [Fig. 5(a)] to a hyperbolic band touched by another hyperbolic band at $\beta = 1.5$ [Fig. 5(b)] and to a bowknot-shaped band touched by a paraboloid band at $\beta = 2$ [Fig. 5(c)]. At $\beta = 1.5$, a strict type-III Dirac point is formed with a flat band crossing a linear band along the k_x direction at $k_y = 0$. Here, we note that the energy of the flat band at $k_y = 0$ remains constant with the parameter β varying, while the dispersive bands shift due to the changed couplings; this reflects the extraordinary robustness of the flat band, as shown in Figs. 5(d)–5(f). The reason for the extraordinary robustness of the flat band is rooted in the decoupling of p_x and p_y modes at $k_y = 0$. The type-III Dirac point with robust flat bands can provide a powerful tool to achieve exotic plaquette states
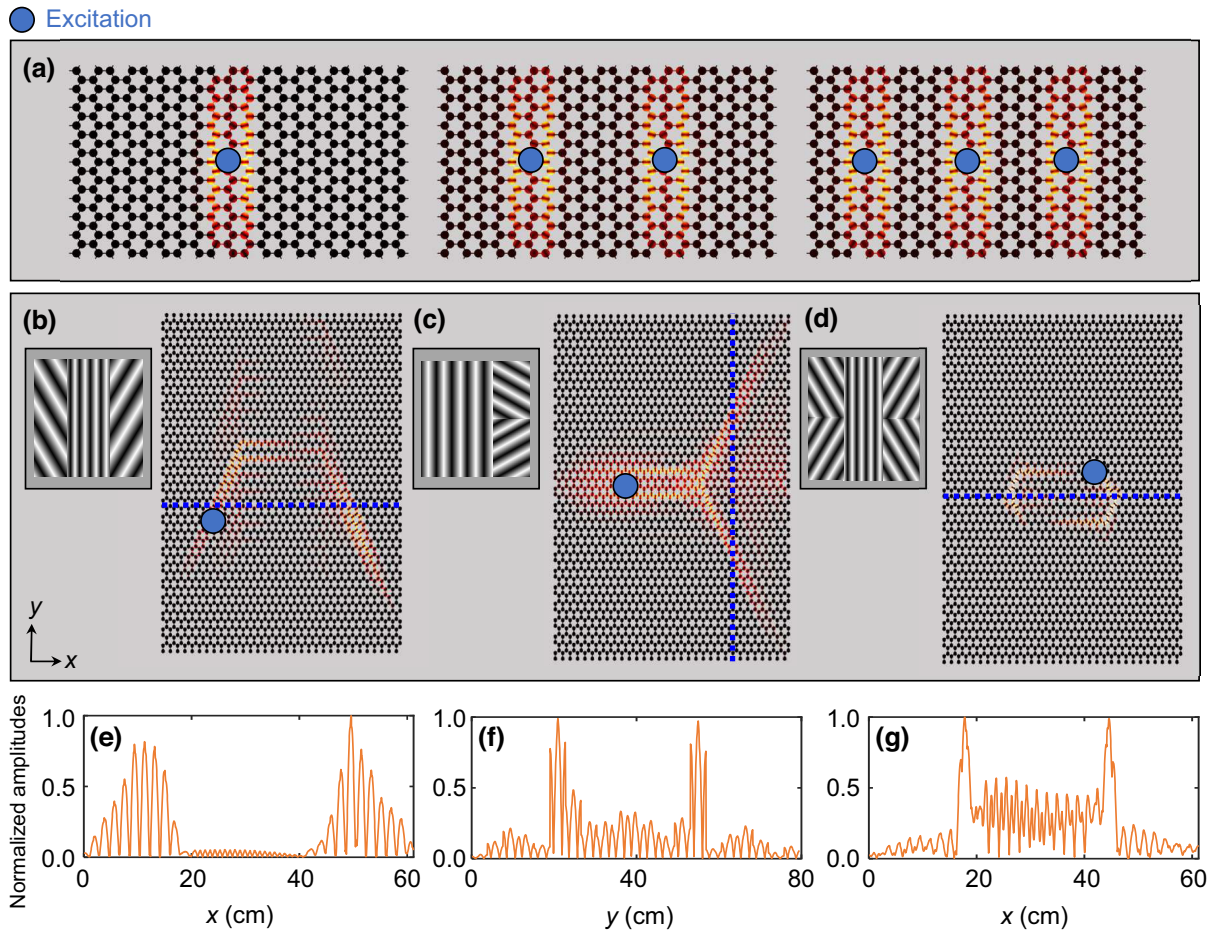
FIG. 7.   Montage operation of plaquette states. (a) Extreme anisotropic wave propagation in the p-orbital lattice at type-III Dirac points, where the property holds for excitations at different positions. (b)–(d) Montage operations of plaquette states by connecting the p-orbital lattices with different principal axes, resulting in three types of sound-wave manipulations, namely, bent-wave routing, splitting, and circulating, respectively. Additional sample points are marked by blue lines for further study. (e)–(g) Normalized pressure amplitudes at the sample points as those marked by blue lines in (b)–(d), respectively.

with diffractionless propagation in a 2D orbital lattice. In Fig. 5(f), another dispersive band appears at the top of the frame, which moves upward in the ideal tight-bonding model, rather than moving downward with increasing β, because the eigenfrequencies of the cavities are perturbed by the varying sizes of the coupling tubes.

IV. MONTAGE OPERATION OF PLAQUETTE STATES

We define the propagation direction of plaquette states in the acoustic orbital lattice as the principal axis. To achieve the montage operation of plaquette states, we further design a unique type of hybrid orbital lattice with differently oriented principal axes in different regions. Here, it needs to be pointed out that the length modulation of coupling tubes will break the translational symmetry of the lattice, which leads to a predicament for constructing

a hybrid orbital lattice. The cross-section modulation of coupling tubes provides an alternative possibility for realizing a hybrid orbital lattice. Specifically, in a unit cell of the orbital lattice, the diameters of coupling tubes along three different directions are labeled w_1, w_2, and w_3, as shown in Fig. 6(a). The relationship between the diameters is determined by factor β. Different relationships between diameters give rise to different directions of the principal axis. For example, when $\beta w_1 = \beta w_2 = w_3$, the lattice is modulated with preserved translational symmetry, for which the principal axis is vertical, as shown at the top of Fig. 6(b). When $w_1 = \beta w_2 = \beta w_3$, the diameters of the coupling tubes (red tubes) along one diagonal direction are β times larger than the ones (blue tubes) in the other diagonal direction, resulting in a 60°-rotated principal axis, as shown in the middle of Fig. 6(b). When $\beta w_1 = w_2 = \beta w_3$, the principal axis is rotated by −60°, as shown in the bottom of Fig. 6(b). The band structures of orbital lattices

at different cross-section modulations are also displayed in Figs. 6(c) and 6(d), which show similar results to the length-modulation case discussed in Fig. 5.

Lastly, the montage of the orbital lattice is investigated. We first focus on the extreme anisotropy of the orbital lattice at the type-III Dirac point. In Fig. 7(a), we put different numbers of dipolar sources in the lattice, where the field distribution indicates the coexistence of multiple plaquette states, as well as the diffractionless propagation of plaquette states. Therefore, by connecting the orbital lattices of differently oriented axes with preserved translational symmetry, it is possible to conduct a montage operation for the plaquette states, where the direction of acoustic waves can be manipulated based on the arrangements of the mosaic lattice. For example, a lattice with the horizontal axis connected by a lattice with a 60° axis at the left and another lattice with a −60° axis at the right enables the bent routing of acoustic waves, as shown in Fig. 7(b). A lattice of the horizontal axis connected by two lattices with 60° and −60° axes at the right serves as a sound splitter, as shown in Fig. 7(c). Moreover, with a more complicated configuration, we can construct a hybrid orbital lattice that supports the whispering-gallery mode of sound, as shown in Fig. 7(d). In Figs. 7(b)–7(d), the acoustic fields are all excited by a single dipolar source, as marked by the blue sphere. In Figs. 7(e)–7(g), the amplitudes of acoustic pressure are extracted at the sample points on the blue lines in Figs. 7(b)–7(d).

V. CONCLUSION

We propose the acoustic realization of strict type-III Dirac points in acoustic orbital lattice and show the existence of plaquette states at the Dirac point. By modulating the orbital lattice with preserved translation symmetry, we further propose the montage operation of plaquette states in an orbital mosaic lattice featuring differently oriented axes in jigsaw regions. Here, we present three examples of acoustic wave routing, splitting, and circulating based on the montage operation of plaquette states. Our results validate the promising properties of orbital lattices, such as decoupling of p_x and p_y modes, which provide a suitable platform for investigating unconventional band structures (e.g., Dirac point, Diabolic point, and flat band) and related wave-propagation dynamics. Our work provides prospects for the exploration of other intriguing domains, such as orbital topological acoustics and non-Hermitian physics [31,32].

ACKNOWLEDGMENTS

[1] O. Bahat-Treidel, O. Peleg, M. Grobman, N. Shapira, M. Segev, and T. Pereg-Barnea, Klein Tunneling in Deformed Honeycomb Lattices, Phys. Rev. Lett. **104**, 063901 (2010).

[2] Y. Zhao, J. Wyrick, F. D. Natterer, J. F. Rodriguez-Nieva, C. Lewandowski, K. Watanabe, T. Taniguchi, L. S. Levitov, N. B. Zhitenev, and J. A. Stroscio, Creating and probing electron whispering-gallery modes in graphene, Science **348**, 672 (2015).

[3] Y. D. Chong, Xiao-Gang Wen, and Marin Soljačić, Effective theory of quadratic degeneracies, Phys. Rev. B **77**, 235125 (2008).

[4] B. A. Bernevig and T. L. Hughes, *Topological Insulators and Topological Superconductors* (Princeton University Press, Princeton, NJ, 2013).

[5] Jungmin Kim, Sunkyu Yu, and Namkyoo Park, Universal Design Platform for an Extended Class of Photonic Dirac Cones, Phys. Rev. Appl. **13**, 044015 (2020).

[6] A. A. Soluyanov, D. Gresch, Z. Wang, Q. Wu, M. Troyer, X. Dai, and B. A. Bernevig, Type-II Weyl semimetals, Nature (London) **527**, 495 (2015).

[7] S. M. Choi, S. H. Jhi, and Y. W. Son, Effects of strain on electronic properties of graphene, Phys. Rev. B **81**, 081407 (2012).

[8] Xiaoxiao Wu, Xin Li, Ruo-Yang Zhang, Xiao Xiang, Jingxuan Tian, Yingzhou Huang, Shuxia Wang, Bo Hou, C. T. Chan, and Weijia Wen, Deterministic Scheme for Two-Dimensional Type-II Dirac Points and Experimental Realization in Acoustics, Phys. Rev. Lett. **124**, 075501 (2020).

[9] M. Goerbig, J.-N. Fuchs, G. Montambaux, and F. Piéchon, Tilted anisotropic Dirac cones in quinoid-type graphene and α-(BEDT-TTF)$_2$I$_3$, Phys. Rev. B **78**, 045415 (2008).

[10] M. Trescher, B. Sbierski, P. W. Brouwer, and E. J. Bergholtz, Quantum transport in Dirac materials: Signatures of tilted and anisotropic Dirac and Weyl cones, Phys. Rev. B **91**, 115135 (2015).

[11] M. Milićević, G. Montambaux, T. Ozawa, O. Jamadi, B. Real, I. Sagnes, A. Lemaître, L. Le Gratiet, A. Harouri, J. Bloch, and A. Amo, Type-III and Tilted Dirac Cones Emerging from Flat Bands in Photonic Orbital Graphene, Phys. Rev. X **9**, 031010 (2019).

[12] A. H. Castro Neto, F. Guinea, N. M. R. Peres, K. S. Novoselov, and A. K. Geim, The electronic properties of graphene, Rev. Mod. Phys. **81**, 109 (2009).

[13] H.-Y. Lu, A. S. Cuamba, S.-Y. Lin, L. Hao, R. Wang, H. Li, Y. Zhao, and C. S. Ting, Tilted anisotropic Dirac cones in partially hydrogenated graphene, Phys. Rev. B **94**, 195423 (2016).

[14] M. Hirata, K. Ishikawa, K. Miyagawa, M. Tamura, C. Berthier, D. Basko, A. Kobayashi, G. Matsuno, and K. Kanoda, Observation of an anisotropic Dirac cone reshaping and ferrimagnetic spin polarization in an organic conductor, Nat. Commun. **7**, 12666 (2016).

[15] T. O'Brien, M. Diez, and C. Beenakker, Magnetic Breakdown and Klein Tunneling in a Type-II Weyl Semimetal, Phys. Rev. Lett. **116**, 236401 (2016).

[16] D. Li, B. Rosenstein, B. Y. Shapiro, and I. Shapiro, Effect of the type-I to type-II Weyl semimetal topological transition on superconductivity, Phys. Rev. B **95**, 094513 (2017).

[17] H.-J. Noh, J. Jeong, E.-J. Cho, K. Kim, B. I. Min, and B.-G. Park, Experimental Realization of Type-II Dirac Fermions

in a PdTe$_2$ Superconductor, Phys. Rev. Lett. **119,** 016401 (2017).

[18] A. Frenzel, C. Homes, Q. Gibson, Y. Shao, K. Post, A. Charnukha, R. J. Cava, and D. Basov, Anisotropic electrodynamics of type-II Weyl semimetal candidate WTe$_2$, Phys. Rev. B **95,** 245140 (2017).

[19] K.-W. Chen, X. Lian, Y. Lai, N. Aryal, Y.-C. Chiu, W. Lan, D. Graf, E. Manousakis, R. Baumbach, and L. Balicas, Bulk Fermi Surfaces of the Dirac Type-II Semimetallic Candidates MAl$_3$ (Where M = V, Nb, and Ta), Phys. Rev. Lett. **120,** 206401 (2018).

[20] F. Fei, X. Bo, R. Wang, B. Wu, J. Jiang, D. Fu, M. Gao, H. Zheng, Y. Chen, and X. Wang, Nontrivial Berry phase and type-II Dirac transport in the layered material PdTe$_2$, Phys. Rev. B **96,** 041201 (2017).

[21] H. Liu, J.-T. Sun, C. Cheng, F. Liu, and S. Meng, Photoinduced Nonequilibrium Topological States in Strained Black Phosphorus, Phys. Rev. Lett. **120,** 237403 (2018).

[22] G. G. Pyrialakos, N. S. Nye, N. V. Kantartzis, and D. N. Christodoulides, Emergence of Type-II Dirac Points in Graphynelike Photonic Lattices, Phys. Rev. Lett. **119,** 113901 (2017).

[23] T. Kawarabayashi, Y. Hatsugai, T. Morimoto, and H. Aoki, Generalized chiral symmetry and stability of zero modes for tilted Dirac cones, Phys. Rev. B **83,** 153414 (2011).

[24] M. Perrot, P. Delplace, and A. Venaille, Topological Transition in Stratified Atmospheres, arXiv:1810.03328.

[25] A. Amo and J. Bloch, Exciton-polaritons in lattices: A nonlinear photonic simulator, C. R. Phys. **17,** 934 (2016).

[26] C. Wu and S. D. Sarma, $p_{x,y}$-Orbital counterpart of graphene: Cold atoms in the honeycomb optical lattice, Phys. Rev. B **77,** 235107 (2008).

[27] T. Jacqmin, I. Carusotto, I. Sagnes, M. Abbarchi, D. D. Solnyshkov, G. Malpuech, E. Galopin, A. Lemaître, J. Bloch, and A. Amo, Direct Observation of Dirac Cones and a Flatband in a Honeycomb Lattice for Polaritons, Phys. Rev. Lett. **112,** 116402 (2014).

[28] G. Zhu and A. Ji, Interaction-driven topological phase transition in a polariton honeycomb optical lattice, Phys. Rev. A **100,** 043608 (2019).

[29] Marta Galbiati, Lydie Ferrier, Dmitry D. Solnyshkov, Dimitrii Tanese, Esther Wertz, Alberto Amo, Marco Abbarchi, Pascale Senellart, Isabelle Sagnes, Aristide Lemaître, Elisabeth Galopin, Guillaume Malpuech, and Jacqueline Bloch, Polariton Condensation in Photonic Molecules, Phys. Rev. Lett. **108,** 126403 (2012).

[30] Shiqi Xia, Ajith Ramachandran, Shiqiang Xia, Denghui Li, Xiuying Liu, Liqin Tang, Yi Hu, Daohong Song, Jingjun Xu, Daniel Leykam, Sergej Flach, and Zhigang Chen, Unconventional Flatband Line States in Photonic Lieb Lattices, Phys. Rev. Lett. **121,** 263902 (2018).

[31] Bo Zhen, Chia Wei Hsu, Yuichi Igarashi, Ling Lu, Ido Kaminer, Adi Pick, Song-Liang Chua, John D. Joannopoulos, and Marin Soljačić, Spawning rings of exceptional points out of Dirac cones, Nature **525,** 354 (2015).

[32] Haoran Xue, Qiang Wang, Baile Zhang, and Y. D. Chong, Non-Hermitian Dirac Cones, Phys. Rev. Lett. **124,** 236403 (2020).